Eksploatacja i Niezawodnosc - Maintenance and Reliability
Volume 29 (2027), Issue 2
https://ein.org.pl

The Polish Maintenance Society

Physics-informed spatiotemporal deep learning for cable fault detection and localization in smart power grids

Xiangfan Su[1,*]

[1] College of Electrical Engineering and Automation, Shandong University of Science and Technology, Qingdao, China
* Corresponding Author: sxfgg12345@163.com

Received: 10 March 2026
Revised: 14 April 2026
Accepted: 30 June 2026
Online: 17 August 2026

Abstract

Reliable detection and localization of cable faults are essential for the secure operation of modern distribution networks, particularly with increasing distributed generation integration. This study proposes a physics-informed spatiotemporal deep learning framework for fault detection and localization in medium-voltage cable systems. The approach embeds telegrapher-equation residual constraints and distributed-generation boundary consistency within a physics-informed neural network to incorporate physical knowledge into the learning process. Long short-term memory networks capture transient temporal features of fault signals, while a topology-aware graph convolutional network identifies the faulted cable section within the network. A physics-regularized regression stage then estimates the precise fault distance inside the identified section. The framework is validated using electromagnetic transient simulations of a 10 kV underground cable network developed in PSCAD/EMTDC under various fault locations, grounding conditions, and distributed generation penetration levels.

Keywords: *deep learning, distributed generation (DG), fault detection, graph neural network (GCN), power grid cable*

Article citation:
Su X, Physics-informed spatiotemporal deep learning for cable fault detection and localization in smart power grids, Eksploatacja i Niezawodnosc – Maintenance and Reliability 2027: 29(2) http://doi.org/10.17531/ein/225297

Highlights

- Developing physics-informed learning for cable fault detection and localization.
- Embedding telegrapher residuals and DG boundary consistency.
- Combining PINN, LSTM, and GCN for unified spatiotemporal localization.
- Achieving 99.6% detection accuracy at 40 dB SNR.

1. Introduction

Cable faults in distribution systems can cause significant service interruptions, equipment damage, and economic losses, especially in urban environments where underground cables dominate [1, 2]. The integration of DG further complicates these events by introducing bidirectional power flows and altering fault transient characteristics [3] These dynamic conditions make fault events harder to distinguish from normal switching operations or DG fluctuations, increasing the challenge of rapid and precise fault handling. Therefore, it is essential to develop reliable approaches that can promptly detect fault occurrence, accurately identify the faulty section, and determine the exact location [4].

Cable fault detection techniques range from traditional reflectometry and impedance analysis to modern machine learning approaches for enhanced monitoring in power systems. Song et al. [5] present time domain reflectometry (TDR) for cable fault location by transmitting a pulse signal into the cable and calculating the time difference between the incident and reflected signals. Building on the TDR principle, Chang et al. [6] and Saleh et al. [7] use compressed or spread-spectrum pulse responses to monitor the condition of cable splices/joints and fault-related signatures.

Frequency domain reflectometry (FDR) employs swept sinusoidal signals to detect local defects through distortion characteristics in the reflected signal spectrum. Norouzi et al. [8] analyze the effect of cable joints on frequency-domain responses, while Shan et al. [9] investigate how segmented thermal aging affects defect location accuracy in XLPE distribution cables; Song et al. [5] also demonstrates time–frequency-domain reflectometry concepts that connect reflectometry responses to faulted locations. Broadband impedance spectroscopy (BIS) applies transmission line theory to assess cable condition by comparing impedance spectra before and after degradation, and Zhang et al. [10] propose a BIS-based method for locating and diagnosing cable abrasion.

Beyond classical reflectometry/impedance techniques, recent studies increasingly emphasize deployment realism and robustness: Ghosh et al. [11] validate travelling-wave fault detection/location using EMT-based testing while explicitly considering measurement-chain limitations, Haohao et al. [12] design an online distributed travelling-wave fault-location scheme for HV cables, and Pan et al. [13] demonstrate incipient-fault identification for 10 kV cables with robustness under low SNR and missing data. In parallel, Baayeh et al. [14] develop an MV cable fault-location method using sheath currents under inverter-based resource operating conditions, Ma et al. [15] introduce a topology-aware graph-convolutional approach for fault localization in distribution networks with high DG penetration, and Uzel et al. [16] present an Optuna-optimized hybrid ANN–RF model for fault detection and classification in transmission systems, reflecting recent trends in automated model selection for protection analytics.

Recent examples include Gashteroodkhani et al. [17], who combine support vector machines with time–frequency-domain features for fault location in hybrid transmission lines with underground cables, and De Xu [18], who develops a semi-supervised hybrid ensemble learning model for detecting faults in 20 kV XLPE cables. Wavelet-based adaptive neuro-fuzzy inference systems have also been explored, as in Veerasamy et al.[19] and Peddakapu et al. [20], for high-impedance and high-voltage direct-current fault detection, respectively.

Recent advances move toward processing raw or minimally processed signals directly. Fu et al. [21] use a deep neural network to detect and locate underground cable faults from resonance frequency responses. Li et al. [22] introduce a Swin Transformer for partial discharge pattern recognition in power cable insulation. Tsotsopoulou et al. [23] develop a deep learning-based scheme for superconducting cable fault location, while Chang and Kwon [24] implement anomaly detection for shielded cables and joints. Wan et al. [25] apply deep belief networks for incipient fault recognition and localization from joint impedance spectra. Said et al. [26] employ a convolutional neural network for underground cable fault classification and location in nuclear facility systems. Swaminathan et al. [27] propose a convolutional neural network–long short-term memory hybrid for simultaneous classification and localization of underground cable faults. For incipient and rare fault detection, Samet et al. [28] propose a similarity-based framework for early-stage fault detection in underground cables. Wang et al. [29] employ stacked autoencoders built on restricted Boltzmann machines to detect insulation faults. Wang et al. [30] combine convolutional neural networks, chaotic systems, and wavelet transforms for fault diagnosis with improved pattern recognition capabilities. Despite advancements in cable fault detection, several limitations remain in existing approaches:

- Limited integration of physical laws in learning frameworks: Most ML-based detection methods lack embedded electrical and propagation physics, leading to reduced interpretability and poorer extrapolation to unseen conditions.
- Dependence on extensive labeled datasets: Supervised deep learning models rely heavily on large annotated datasets, which are difficult to obtain for rare or incipient fault scenarios.
- Lack of unified detection and localization frameworks: Many methods focus solely on classification without integrating precise fault localization into the same model pipeline.

To address the identified gaps, this work makes the following key contributions:

1. Unified detection–section identification–distance localization pipeline: We develop an integrated learning pipeline that performs fault detection, identifies the faulted cable section using topology-aware spatial cues, and estimates the continuous fault distance within the identified section, avoiding fragmented multi-tool workflows.

2. Reduced dependence on large labeled datasets through physics-guided training: By enforcing telegrapher-equation residual constraints and distributed-generation boundary consistency, the proposed method remains accurate under reduced labeled training data, as validated by the 50% and 25%

training-set experiments.

3. Physics- and boundary-consistent learning under distributed generation: We incorporate traveling-wave propagation physics and distributed-generation boundary behavior into learning so that predictions remain physically consistent under bidirectional fault currents and varying operating states.

4. Robustness under realistic sensing constraints: We quantify performance under practical measurement limitations including different noise levels, bandwidth limitation, sensor timing misalignment, and missing/unreliable sensors, and we evaluate how accuracy improves with denser instrumentation.

The paper is structured as follows: Section 2 presents the governing physics equations and constraints that form the foundation for modeling transient fault behavior in cable networks. Section 3 describes the proposed PINN–LSTM–GCN framework, detailing the integration of physics-informed modeling, temporal feature extraction, and spatial topology learning. Section 4 provides the simulation setup and results, including performance evaluation, robustness analysis, and comparisons with baseline methods. Section 5 concludes the work with key findings, practical implications, and future research directions.

2. Physics equations and constraints

This section establishes the physical foundations that underpin the proposed fault detection and localization framework. The framework relies on the transmission-line (TL) modeling of medium-voltage (MV) power cables, which governs how electrical transients (such as fault-generated traveling waves) propagate along the network [31].

Because fault-triggered traveling waves contain components from several kHz to hundreds of kHz (depending on cable length and sensor bandwidth), a distributed-parameter TL model is adopted. The proposed physics constraints enforce the telegrapher PDE residuals over the same band implicitly captured by the PSCAD electromagnetic transient simulation and the measurement preprocessing described in Section 4. By embedding these governing equations into the learning process, the model remains consistent with the underlying electrical laws, even in the presence of DG units that introduce bidirectional power flow and dynamic impedance changes.

2.1. Telegrapher's equations for cable modeling

When the transient wavelength is short compared to the cable length-as in partial discharge (PD) or faultinduced high-frequency (HF) events-the transmission-line theory is essential. The cable is modeled as an infinitely divisible chain of uniform segments of length Δz (See Figure 1), each characterized by primary constants: resistance $R'[\Omega/\mathrm{m}]$, inductance $L'[\mathrm{H/m}]$, conductance $G'[\mathrm{S/m}]$, and capacitance $C'[\mathrm{F/m}]$. Applying Kirchhoff's voltage and current laws to an infinitesimal segment yields the time-domain telegrapher's equations:

$$-\frac{\partial u(z,t)}{\partial z} = R' i(z,t) + L' \frac{\partial i(z,t)}{\partial t} \tag{1}$$

$$-\frac{\partial i(z,t)}{\partial z} = G' u(z,t) + C' \frac{\partial u(z,t)}{\partial t} \tag{2}$$

Applying the Fourier transform in time, $u(z,t) \leftrightarrow U(z,\omega)$ and $i(z,t) \leftrightarrow I(z,\omega)$, yields the frequency domain form:

$$-\frac{\partial U(z)}{\partial z} = (R' + j\omega L')I(z) = Z'(\omega)I(z) \tag{3}$$

$$-\frac{\partial I(z)}{\partial z} = (G' + j\omega C')U(z) = Y'(\omega)U(z) \tag{4}$$

Note that $R'(\omega), L'(\omega), C'(\omega)$, and $G'(\omega)$ may be frequency dependent due to skin/proximity effects and dielectric polarization;

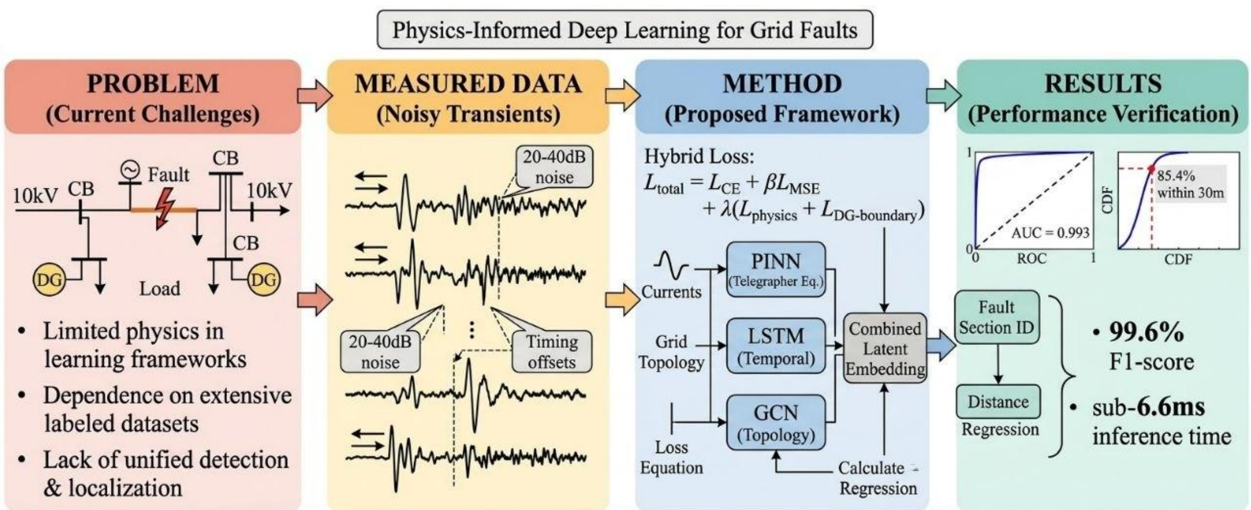

therefore $Z'(\omega), Y'(\omega)$, and $\gamma(\omega)$ capture realistic attenuation/dispersion. Eliminating either variable yields the wave equations:

$$\frac{\partial^2 U(z)}{\partial z^2} = \gamma^2 U(z) \tag{5}$$

$$\frac{\partial^2 I(z)}{\partial z^2} = \gamma^2 I(z) \tag{6}$$

where the propagation constant $\gamma = \alpha + j\beta$ captures both attenuation $\alpha[\mathrm{Np/m}]$ and phase shift $\beta[\mathrm{rad/m}]$. These relations define the physics constraints used later in the PINN loss function.

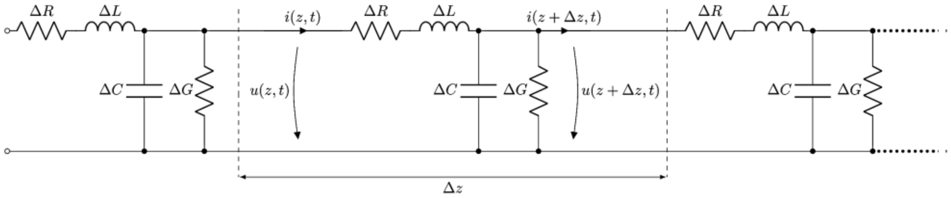

Figure 1. Distributed-parameter model of a cable section.

2.2. Boundary conditions, reflection effects, and DG penetration

The general solution to the wave equations is the superposition of forward- and backward-traveling waves:

$$U(z,\omega) = U_f(\omega)e^{-\gamma(\omega)z} + U_b(\omega)e^{\gamma(\omega)z}, I(z,\omega) = I_f(\omega)e^{-\gamma(\omega)z} + I_b(\omega)e^{\gamma(\omega)z} \tag{7}$$

These are related by the characteristic impedance:

$$Z_c = \sqrt{\frac{Z'}{Y'}} = \frac{U_f}{I_f} = -\frac{U_b}{I_b} \tag{8}$$

At discontinuities-such as terminations, joints, faults, or DG interconnection points-part of the wave is reflected, with reflection coefficient:

$$r_z = \frac{Z_z - Z_c}{Z_z + Z_c} \tag{9}$$

At a DG interconnection node, the effective termination $Z_z(\omega)$ is replaced by an equivalent small-signal impedance $Z_{DG}(\omega)$ (or equivalently a Norton injection), which depends on the DG control mode (PQ/PV/droop) and interfacing dynamics. In this work, DG influence is represented through an injected current term and boundary residuals (Section 3.1), allowing the learning model to remain consistent with KCL/KVL under bidirectional fault currents. The boundary conditions at DG locations must satisfy Kirchhoff's laws with current and voltage injection:

$$I_{\mathrm{left}}(z_s,t) + I_{\mathrm{DG}}(t) = I_{\mathrm{right}}(z_s,t), \qquad U_{\mathrm{left}}(z_s,t) = U_{\mathrm{right}}(z_s,t) \tag{10}$$

Here z_s denotes the DG connection point. Where $I_{\mathrm{DG}}(t)$ denotes the equivalent injection current arising from the DG operating state and interface/controller dynamics. These DG-modified boundaries influence both the magnitude and polarity of reflected waves, and must be explicitly modeled to maintain fault location accuracy under bidirectional power flows (See Figure 2).

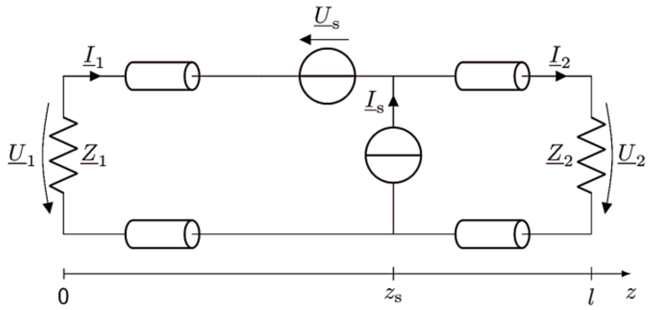

Figure 2. Schematic of a terminated cable with a transient source located at an arbitrary point z_s.

2.3. Cable impedance models and material parameters

The propagation constant γ and characteristic impedance Z_c are determined from the primary line constants, which depend on cable geometry and material properties (See Figure 3). In the simulations, the per-unit-length parameters are obtained from standard XLPE cable geometry/material data (manufacturer datasheets or typical MV cable parameter ranges) and used consistently in the PSCAD frequency-dependent cable model and in the physics residual evaluation. For a single-phase MV XLPE cable with conductor radius r_1, inner semiconductor thickness d_{scl}, insulation thickness d_{ins}, outer semiconductor thickness d_{sc2}, and outer conductor inner radius r_2, the conductor resistance at DC is:

$$R'_{\mathrm{DC}} = \frac{1}{\sigma_{\mathrm{co}} A} \tag{11}$$

At HF, the skin depth

$$\delta = \sqrt{\frac{2}{\sigma_{\mathrm{co}} \omega \mu_0 \mu_{\mathrm{co}}}} \tag{12}$$

reduces the effective cross-section, increasing R' to approximately:

$$R'_{\mathrm{AC}} \approx \frac{1}{\sigma_{\mathrm{co}} 2\pi r_1 \delta} \tag{13}$$

The inductance and capacitance per unit length are:

$$L' \approx \frac{\mu_0 \mu_{\mathrm{co}}}{2\pi} \ln\left(\frac{r_2}{r_1}\right), C' = \frac{2\pi \varepsilon_0 \varepsilon(\omega)}{\ln\left(\frac{r_2}{r_1}\right)} \tag{14}$$

where $\varepsilon(\omega) = \varepsilon'(\omega) + j\varepsilon''(\omega)$ models dielectric polarization and loss. G' is estimated from dielectric loss in high-quality XLPE insulation. The expressions in (11)–(14) provide a compact physical parameterization; in practice, proximity effects and screen/sheath coupling can further modify $R'(\omega)$ and $L'(\omega)$. These effects are captured in the EMT simulation model (Section 4) and are treated as part of the physics-consistent data generation; the PINN residuals regularize the learned fields against the governing PDE structure.

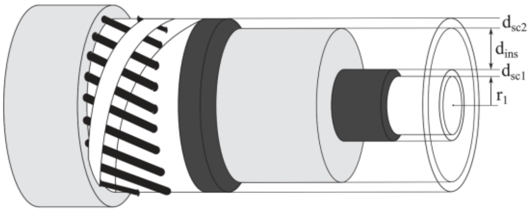

Figure 3. Cross-section of a typical single-phase medium-voltage XLPE-insulated cable.

2.4. Physical constraints in learning models with DG integration

The telegrapher's equations and impedance–admittance models describe how voltage and current waves propagate, attenuate, and reflect. Faults introduce abrupt impedance changes, while DG units create dynamic injection points that alter wave propagation paths. The magnitude, polarity, and arrival time of traveling waves depend jointly on:

1. Cable parameters (R^',L^',C^',G^'),
2. Material frequency dependence,
3. Boundary conditions at faults, terminations, and DG nodes.

In practical deployments, measured transients are affected by sensor bandwidth limits, sampling/anti-alias filtering, additive noise and interference, and synchronization errors between distributed measurement nodes. These effects do not alter the underlying propagation physics, but they distort the observed waveforms. Accordingly, the proposed framework combines physics residual constraints with temporal–spatial learning, and Section 4 evaluates robustness under reduced SNR, bandwidth-limited measurements, and missing/weak sensor observations.

Finally, because propagation and attenuation depend on both geometry and electrical parameters, spatial correlations between nodes are influenced not only by physical distance but also by cable impedance, branching, and boundary conditions—motivating topology-aware learning (Section 3.3).

3. Proposed framework

3.1. Physics-guided component

The dynamic behavior of traveling waves along a power cable is governed by the telegrapher's equations, which couple the spatial and temporal variations of voltage $u(z,t)$ and current $i(z,t)$ along the line. These equations, expressed in Eqs. (1)-(14), remain valid in the presence of distributed generation (DG), but DG units act as additional dynamic injection points that modify local boundary conditions and alter the propagation, attenuation, and reflection of traveling waves. In the proposed framework, the telegrapher's equations are directly embedded into a Physics-Informed Neural Network (PINN), with outputs assigned physical meaning such that $\hat{u}(z,t;\theta) \approx u(z,t)$ and $\hat{\imath}(z,t;\theta) \approx i(z,t)$, where θ denotes the trainable parameters. Automatic differentiation computes $\partial\hat{u}/\partial z, \partial\hat{\imath}/\partial z, \partial\hat{u}/\partial t$, and $\partial\hat{\imath}/\partial t$, enabling direct evaluation of the telegrapher's equations within the learning loop.

In our implementation, the network predicts $\hat{u}$ and $\hat{\imath}$ at the measurement nodes over the analysis window (discrete space-time samples). Physics residuals are evaluated using automatic differentiation with respect to the space coordinate along each cable segment and time t_t at collocation points (z_j, t_j) chosen within the corresponding cable section. Thus, the PINN acts as a physics-regularized signal model coupled to the classification heads described in Section 3.4.

To account for DG effects, additional DG boundary residuals are introduced at DG node locations, enforcing

Kirchhoff's voltage and current laws with injected DG active/reactive power. This ensures that both voltage and current waveforms remain physically consistent even under bidirectional flows. The residuals for the voltage and current equations are:

$$R_u(z,t) = -\frac{\partial \hat{u}}{\partial z} - \left(R'\hat{\imath} + L'\frac{\partial \hat{\imath}}{\partial t}\right) \tag{15}$$

$$R_i(z,t) = -\frac{\partial \hat{\imath}}{\partial z} - \left(G'\hat{u} + C'\frac{\partial \hat{u}}{\partial t}\right) + I_{\mathrm{DG}}(z,t) \tag{16}$$

$I_{\mathrm{DG}}(z,t)$ is nonzero only at DG interconnection locations (modeled as equivalent injected currents determined by DG operating state in the EMT simulation), and is zero elsewhere. The physics loss is computed over N_f collocation points (z_j, t_j) as:

$$L_{\text{physics}} = \frac{1}{N_f}\sum_{j=1}^{N_f}\left(\left\|R_u(z_j,t_j)\right\|^2 + \left\|R_i(z_j,t_j)\right\|^2\right) \tag{17}$$

Similarly, the data loss over N_u measured points is:

$$L_{\text{MSE}} = \frac{1}{N_u}\sum_{k=1}^{N_u}\left(\|\hat{u}(z_k,t_k) - u_{\text{meas}}(z_k,t_k)\|^2 + \|\hat{\imath}(z_k,t_k) - i_{\text{meas}}(z_k,t_k)\|^2\right) \tag{18}$$

$$L_{DG-\,boundary} = \frac{1}{N_{DG}}\sum_{m=1}^{N_{DG}}\left(\left\|\hat{U}_{left}(z_m,t) - \hat{U}_{right}(z_m,t)\right\|^2 + \left\|\hat{I}_{left}(z_m,t) + I_{DG}(t) - \hat{I}_{right}(z_m,t)\right\|^2\right) \tag{19}$$

$L_{DG-\,boundary}$ enforces voltage continuity and current balance at DG nodes, ensuring physically consistent wave interactions under bidirectional flows. The total hybrid loss is:

$$L_{\text{total}} = L_{CE} + \beta L_{\text{MSE}} + \lambda\left(L_{\text{physics}} + L_{\text{DG-boundary}}\right) \tag{20}$$

L_{CE} supervises fault section classification, L_{MSE} optionally supervises reconstructed voltage/current signals at measurement nodes, and λ controls the strength of physics regularization; β is set via validation. $L_{\text{DG-boundary}}$ enforces DG-related constraints. This formulation enables the model to generalize effectively to unseen DG penetration levels and diverse fault scenarios while maintaining physical interpretability and robustness to noise.

3.2. Data-driven temporal feature extraction

In the proposed framework, the LSTM network serves as the temporal feature extraction module, enabling the model to capture the dynamic evolution of fault transients in distribution cables, particularly under the operational variability introduced by DG. The LSTM's ability to preserve relevant historical information while filtering out noise makes it well-suited for analyzing the sequential voltage and current waveforms measured at multiple points in the network following a fault event. At each time step t, the LSTM processes the current measurement vector X_t together with the hidden state h_{t-1} and cell state C_{t-1} from the previous step to produce updated states h_t and C_t. The gating mechanism regulates the memory flow: the forget gate f_t determines the proportion of prior information to retain, the input gate i_t controls the extent of new information stored, and the output gate o_t decides how much of the updated memory is exposed to the next layer. The operations are given by:

$$i_t = \sigma(W_i \cdot [h_{t-1}, X_t] + b_i) \tag{21}$$

$$f_t = \sigma\left(W_f \cdot [h_{t-1}, X_t] + b_f\right) \tag{22}$$

$$\tilde{C}_t = \tanh(W_C \cdot [h_{t-1}, X_t] + b_C) \tag{23}$$

$$o_t = \sigma(W_o \cdot [h_{t-1}, X_t] + b_o) \tag{24}$$

where $W_{\{\cdot\}}$ and $b_{\{\cdot\}}$ are the trainable weights and biases, $\sigma(\cdot)$ denotes the sigmoid activation, and $\tanh(\cdot)$ is the hyperbolic tangent function. The updated cell and hidden states are:

$$C_t = f_t \odot C_{t-1} + i_t \odot \tilde{C}_t \tag{25}$$

$$h_t = o_t \odot \tanh(C_t) \tag{26}$$

With $\odot$ representing element-wise multiplication. In this work, three stacked LSTM layers (80, 50, and 30 memory cells) are employed to extract multi-level temporal representations of the transient waveforms. Dropout layers are inserted between LSTM layers to reduce overfitting and enhance generalization to unseen DG operating conditions. The final LSTM output is passed to a fully connected layer, the size of which corresponds to the number of target fault categories for the given stage of the detection–localization pipeline. A softmax activation produces probability distributions over fault types, faulted sections, or precise fault locations depending on the stage.

The model is trained using the Adam optimizer with a learning rate of 10^{-3}, batch size tuned to balance accuracy and training efficiency, and early stopping to prevent overfitting. Training utilizes sequentially organized traveling-wave data collected under diverse DG penetration scenarios, ensuring that the LSTM learns to recognize temporal patterns robust to power injections from multiple sources. By learning long-term temporal dependencies inherent in fault transients-while the preceding PINN module enforces physical consistency-the LSTM ensures that subtle waveform variations caused by fault type, location, and DG operating state are accurately preserved for subsequent spatial dependency modeling.

3.3. Spatial dependency modeling

After temporal features are extracted from each sensor location using the LSTM network, the next objective is to exploit the spatial dependencies between different points in the cable network. Fault-induced transients rarely remain confined to a single location; instead, they propagate along the connected cable segments, influencing voltage and current waveforms at neighboring measurement points. To capture this spatial correlation, the distribution network is modeled as an undirected weighted graph $G = (V, E, W)$, where each node $v_i \in V$ represents a measurement point (such as a bus or joint with available voltage/current sensors), and each edge $(v_i, v_j) \in E$ represents a physical cable connection between two points. The weighted adjacency matrix $W \in \mathbb{R}^{n\times n}$ encodes the strength of connection between nodes. In our case, W_{ij} is computed from the shortest physical distance between points i and j, transformed using a Gaussian kernel:

$$W_{ij} = \exp\left(-\frac{S_{ij}^2}{\sigma_S^2}\right) \tag{27}$$

where S_{ij} is the shortest-path distance and σ_S is a scaling parameter controlling neighborhood influence. While a distance-based Gaussian kernel is an effective proxy for proximity, practical spatial correlations are also shaped by cable impedance parameters, branching topology, sensor bandwidth/synchronization, and DG-dependent boundary behavior. To account for this, we additionally consider an electrical-distance variant where S_{ij} is replaced by a path-impedance or propagation-delay distance; Section 4.4 evaluates the impact of distance-based versus electrical-distance weighting on section identification and localization. This ensures that nearby nodes have higher connection weights, while distant nodes contribute less to each other's feature updates. From W, the degree matrix D is computed with $D_{ii} = \sum_j W_{ij}$, and the normalized Laplacian is obtained as:

$$\Delta = I - D^{-1/2} W D^{-1/2} \tag{28}$$

The Laplacian encapsulates the network topology and is the foundation for spectral graph convolution. The idea of spectral convolution is to transform node features into the graph Fourier domain, apply a filter, and transform back. Since direct computation is expensive, we use a Chebyshev polynomial approximation to make the convolution localized and efficient:

$$h_\alpha(\Lambda) = \sum_{k=0}^{K} \alpha_k T_k(\tilde{\Lambda}) \tag{29}$$

where α_k are learnable parameters, T_k are Chebyshev polynomials, and $\tilde{\Lambda} = \frac{2\Lambda}{\lambda_{\max}} - I$ scales the eigenvalues to $[-1,1]$. The recursive form:

$$T_k(x) = 2xT_{k-1}(x) - T_{k-2}(x), T_0 = 1, T_1 = x \tag{30}$$

allows us to compute localized filtering up to K hops without full eigendecomposition. For the input to the GCN, the LSTM output matrix $\mathbf{X} \in \mathbb{R}^{n\times F}$ (where n is the number of nodes and F is the number of temporal features per node) serves as the node feature matrix. A single GCN layer updates node features as:

$$\mathrm{H}^{(l+1)} = \sigma\left(\sum_{k=0}^{K} T_k(\tilde{\Delta}) \mathrm{H}^{(l)} \Theta_k\right) \tag{31}$$

where Θ_k are trainable weight matrices and $\sigma(\cdot)$ is a nonlinear activation function (ReLU). By integrating the network topology into the learning process, the GCN ensures that fault localization is not based solely on local waveform distortions but also considers how these distortions propagate spatially through the network. This allows the model to:

- Correctly identify faults even with partial or noisy measurements.
- Distinguish between physically close but electrically isolated sections.
- Improve generalization across varying DG operating points and fault types.

3.4. Integrated physics–temporal–spatial learning framework

The proposed framework is designed as a unified learning pipeline that integrates temporal sequence modeling, spatial topology learning, and physics-based regularization for accurate and physically consistent faulty section identification. At its core, the method uses LSTM to capture time-domain transient patterns, GCN to model spatial correlations across the cable network, and a PINN-based physics constraint to ensure electromagnetic consistency with the telegrapher's equations. Operational Flow:

1. Temporal Feature Extraction (LSTM): The raw voltage-current time series from all measurement nodes are first passed through an LSTM. This module learns sequential dependencies and captures transient signatures immediately after a fault event. The output is a temporal embedding $H_0^{(n)}$ for each sample n.
2. Spatial Aggregation (GCN): The temporal embeddings are then fed into a GCN that operates over the cable network's weighted adjacency matrix A. Here, spatial correlations are learned by propagating feature information along physical cable connections, allowing the network to account for the way faults influence neighboring nodes.
3. Faulty Section Prediction (Fully Connected + Softmax): The GCN output is processed by fully connected layers to produce a probability distribution $\hat{y}^{(n)}$ over possible fault sections.
4. Physics Residual Computation (PINN): In parallel, the predicted voltage $\hat{u}$ and current $\hat{\imath}$ fields are passed through a PINN residual block, where the telegrapher's equations are evaluated at selected space-time collocation points (z_j, t_j). This yields residuals $R_{u,j}$ and $R_{i,j}$ that measure how well the predictions satisfy physical laws.
5. Loss Computation:
   - Data Loss: Cross-entropy between predicted probabilities and ground-truth section labels.
   - Physics Loss: Mean squared residuals of the telegrapher's equations.
   - Hybrid Loss: $L_{\text{total}} = L_{CE} + \beta L_{\text{MSE}} + \lambda(L_{\text{physics}} + L_{\text{DG-boundary}})$. λ is selected via a validation sweep to balance convergence stability and generalization; Section 4.3 includes a sensitivity analysis of detection F1/AUC and localization MAE versus λ.
6. Parameter Update: All network parameters $\Theta_{\text{LSTM}}, \Theta_{\text{GCN}}, \Theta_{\text{FC}}$ are jointly updated using an optimizer (Adam), ensuring that temporal, spatial, and physics constraints are optimized together.

The pseudocode operates as an integrated learning loop that unifies temporal, spatial, and physics-based constraints (see algorithm 1). The process begins with initialization, where the model parameters are either set randomly or loaded from pre-trained weights, and the key hyperparameters λ (which balances the physics-based regularization) and η (the learning rate) are defined. The outer loop runs across multiple epochs, enabling the model to refine its parameters through repeated exposure to the training dataset. Within each epoch, an inner loop processes smaller data batches, which improves computational efficiency and accelerates convergence. In steps (1)–(3), the raw voltage–current time series are sequentially passed through the LSTM to extract temporal features, the GCN to capture spatial dependencies within the cable network topology, and finally fully connected layers with a softmax activation to produce classification probabilities for each possible fault section. In step (4), the classification error is calculated using a cross-entropy loss function. Steps (5)–(6) enforce the physics constraints by computing the residuals of the telegrapher's equations at specified space–time collocation points, followed by averaging these residuals to obtain the physics loss. In step (7), the classification loss and the physics loss are combined into a single objective function weighted by λ. Step (8) updates the model parameters using gradient-based optimization, Adam. Once training concludes, the inference stage determines the most probable faulty section by selecting the class index with the highest predicted probability.

After Stage-1 identifies the most probable faulted section, Stage-2 estimates the continuous fault distance within that section. This stage uses the same temporal encoder (LSTM) and physics regularization, with a regression head that outputs the normalized distance $\hat{d}$ along the selected section. The regression loss is defined as an ℓ1 or ℓ2 error against the true distance, and the telegrapher residual terms remain active to preserve physical consistency.

Algorithm 1. Training loop for Stage-1 faulty section identification (LSTM–GCN with physics regularization)

Let $X^{(n)}$ be synchronized voltage-current time series at all measured nodes for sample n, A the weighted adjacency (graph) matrix, and $\Theta_{\text{LSTM}}, \Theta_{\text{GCN}}, \Theta_{\text{FC}}$ the trainable parameters.

Initialize: $\Theta_{\text{LSTM}}, \Theta_{\text{GCN}}, \Theta_{\text{FC}}, \lambda > 0, \eta > 0$

for epoch = 1: E do

for batch $B \subset \{1, \dots, N_{\text{train}}\}$ do

(1) $H_0^{(n)} \leftarrow \text{LSTM}\big(X^{(n)}; \Theta_{\text{LSTM}}\big), \forall n \in B$

(2) $H_L^{(n)} \leftarrow \text{GCN}\big(H_0^{(n)}, A; \Theta_{\text{GCN}}\big), \forall n \in B$

(3) $\hat{y}^{(n)} \leftarrow \text{Softmax}\Big(\text{FC}\big(H_L^{(n)}; \Theta_{\text{FC}}\big)\Big)$

(4) $L_{\text{MSE}} \leftarrow -\frac{1}{|B|}\sum_{n\in B}\sum_{c=1}^{C} y_c^{(n)} \log \hat{y}_c^{(n)}$

(5) Obtain $\hat{u}^j, \hat{\imath}^j$ at collocation point (z_j, t_j) from the physics-regularized signal head (PINN block) driven by the latent embedding of sample n.

$R_{u,j} \leftarrow -\partial_z \hat{u}^j - (R'\hat{\imath}^j + L'\partial_t \hat{\imath}^j)$

$R_{i,j} \leftarrow -\partial_z \hat{\imath}^j - (G'\hat{u}^j + C'\partial_t \hat{u}^j) + I_{\text{DG}}(z,t)$

(6) $L_{\text{physics}} \leftarrow \frac{1}{N_f}\sum_{j=1}^{N_f}\left(\left\|R_{u,j}\right\|_2^2 + \left\|R_{i,j}\right\|_2^2\right)$

(7) $L_{\text{total}} = L_{CE} + \beta L_{\text{MSE}} + \lambda\big(L_{\text{physics}} + L_{\text{DG-boundary}}\big)$

(8) $(\Theta_{\text{LSTM}}, \Theta_{\text{GCN}}, \Theta_{\text{FC}}) \leftarrow (\Theta_{\text{LSTM}}, \Theta_{\text{GCN}}, \Theta_{\text{FC}}) - \eta\nabla L_{\text{total}}$

end for

end for

Inference: $\hat{s} \leftarrow \arg\max_{c} \hat{y}_c$ (faulty section index)

To improve robustness under limited instrumentation, we train with random node dropout (sensor masking) so the GCN learns stable aggregation when one or more measurement nodes are missing or unreliable. During inference, missing nodes are masked and excluded from aggregation. Section 4 quantifies performance degradation versus the number of missing sensors.

4. Simulation and results

To evaluate the effectiveness of the proposed framework, we simulate a medium-voltage (10 kV) underground cable distribution network in PSCAD/EMTDC. The test network, depicted in Figure 4, consists of three feeders connected via circuit breakers CB1–CB5 and incorporating 24 load points (L1–L24). The measurement points serve as the graph nodes for the GCN module, while the physical connections between cables define the graph adjacency matrix. All measurements collected in three edge nodes (EN1, EN2, and EN3), we get measurements from them. In the base sensing configuration, three measurement units are installed at EN1–EN3. For graph learning, only instrumented nodes are treated as observed nodes; non-instrumented buses are unobserved. Section 4.4 further evaluates denser sensing (two sensors per feeder) and missing-sensor scenarios. All cables are grounded at both ends through grounding lines with a resistance of 1.0 Ω. The system is capable of switching between multiple neutral grounding configurations via switch K1 to test robustness under different fault grounding modes.

A diverse set of fault scenarios are simulated to capture variations in location, DG penetration, grounding mode, and electrical severity. Fault locations span distances from 100 m to 2000 m from the sending node, with R_{FS} (core-to-sheath resistance) ranging from 10 Ω to 100 Ω,R_FG (sheath-to-ground resistance) varying between 100 Ω and 400 Ω, and inception angles (θ_f) covering 30^∘ to 90^∘. These cases encompass both moderate and severe disturbances under ungrounded (UNG) and arc-suppression coil grounded (ASG) configurations, enabling a comprehensive evaluation of detection robustness. Voltage and current transients are recorded at all monitored nodes, and gaussian noise is superimposed to emulate sensor imperfections. To evaluate noise robustness, we generate datasets at SNR = 40/30/20 dB and report performance under each level. Each captured waveform is segmented into a fixed 200 ms window, normalized to its pre-fault RMS value, and augmented via temporal shifting to enhance generalization capability. The dataset is divided into 70% for training, 15% for validation, and 15% for testing.

PSCAD/EMTDC electromagnetic transient simulation captures traveling-wave propagation under distributed-parameter cable modeling, including attenuation and dispersion consistent with RLGC behavior. To reflect practical measurement chains, Section 4.4 additionally evaluates bandwidth-limited measurements (anti-alias filtering), timing misalignment between sensors, and non-ideal/noisy observations. These tests provide bounds on expected performance under realistic sensor constraints.

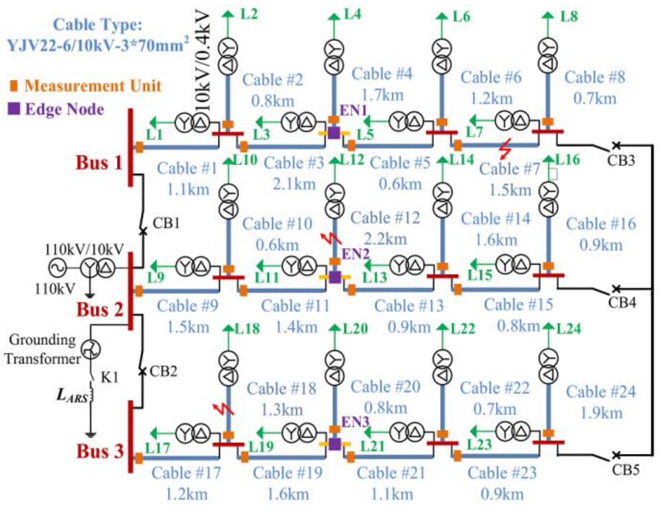

Figure 4. Diagram of the simulated 10 kV distribution cable

network.

Before evaluating classification accuracy, it is important to examine how different fault scenarios influence the measured voltage and current waveforms. Figures 5 and 6 illustrate representative grounding line current responses captured at EN1-EN3 for three simulated fault conditions in the 10 kV distribution network. The first case involves a fault on cable #7 with $R_{FS} = 10\Omega, R_{FG} = 190\Omega$, a fault inception angle of 30°, and a fault distance of 498 m. The second case corresponds to a fault on cable #12 under arc-suppression coil grounding, with $R_{FS} = 10\Omega, R_{FG} = 10^3\Omega$, a 30° inception angle, and a distance of 1475 m. The third case involves a fault on cable #18 with $R_{FS} = 100\Omega, R_{FG} = 400\Omega$, a 90° inception angle, and a distance of 721 m. The results reveal a clear signature: for cables directly involved in the fault, the current magnitude rises sharply within 1–2 ms of fault inception, while upstream cables exhibit currents in the same direction and downstream cables show opposite polarity. This polarity reversal provides a strong spatial cue that the GCN exploits during graph-based aggregation.

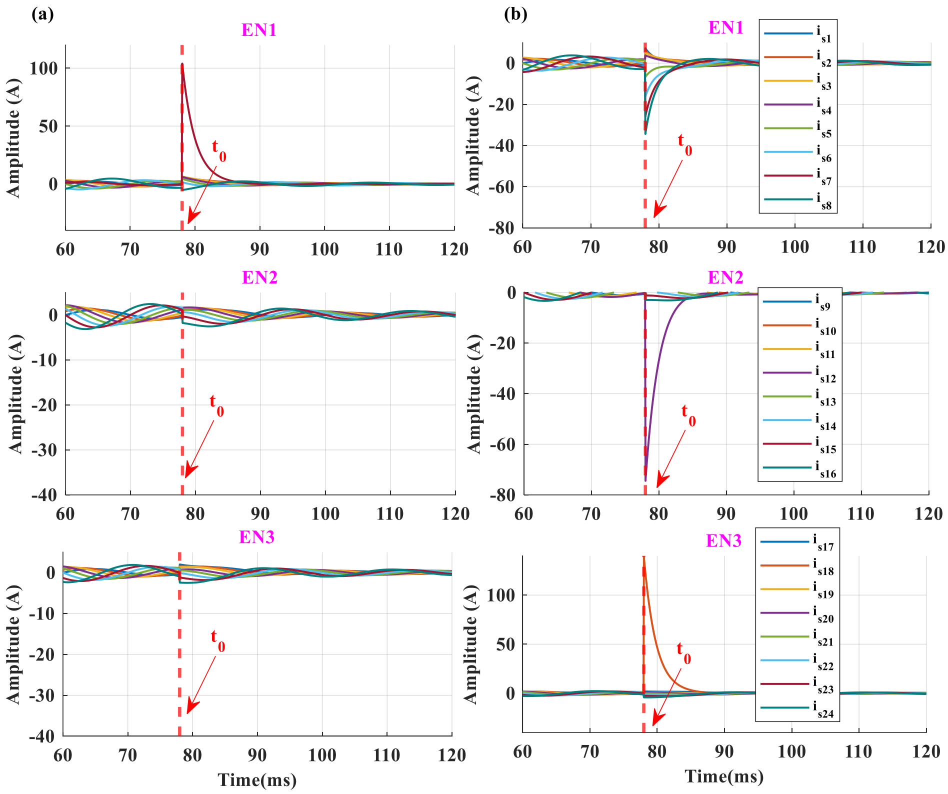

Figure 5. Initial measured current waveforms a) first case, b) second case.

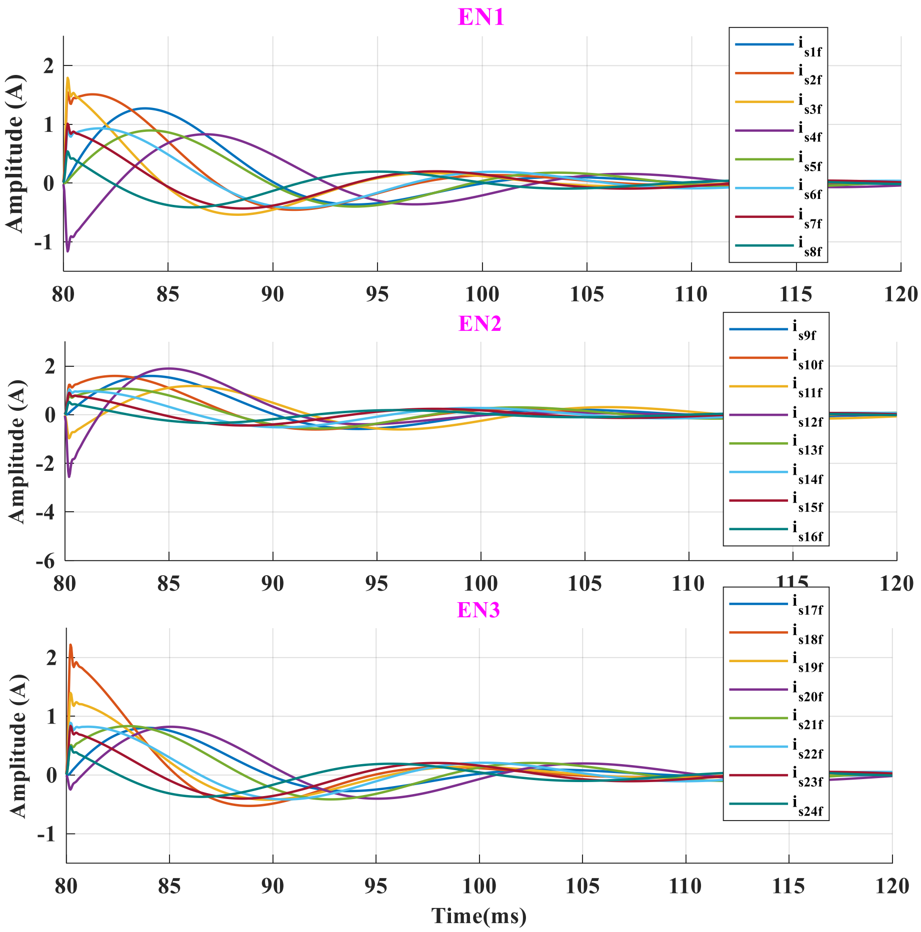

Figure 6. Filtered measured current waveforms in third case.

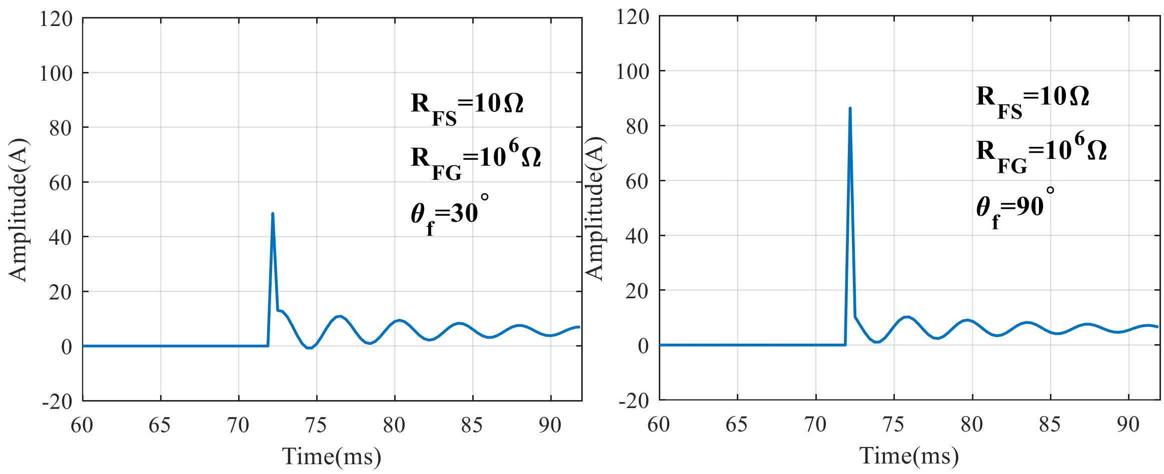

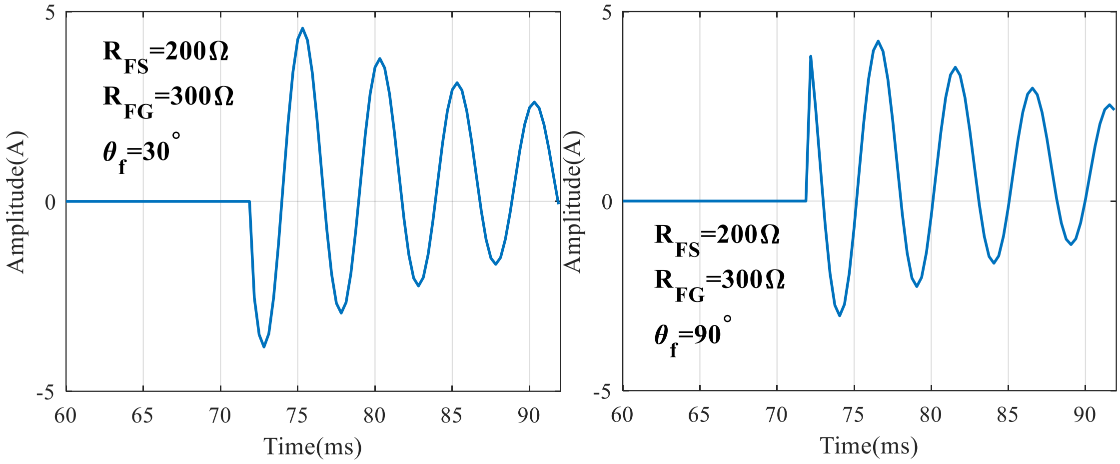

Figure 7. Measured currents at cable #21 under different fault condition.

Figure 7 shows the grounding line currents at the local end of faulted cable #21 under four different fault conditions, combining variations in fault resistance (R_{FS}) and inception angle (θ_f). The results indicate that both parameters significantly influence the transient response. Lower fault resistances produce higher current peaks, while higher resistances yield reduced amplitudes and more pronounced oscillatory decay. Similarly, the inception angle affects the initial polarity and shape of the waveform, altering the transient's symmetry and zero-crossing behavior. These sensitivities highlight the importance of capturing both parameters in fault detection and localization models.

4.1. Fault detection accuracy

Table 1 presents the fault detection performance of the proposed PINN–LSTM–GCN framework under varying noise levels. At a high SNR of 40 dB, the model achieved 99.6% accuracy, 99.4% precision, 99.7% recall, and a 99.6% F1-score. Even at moderate (30 dB) and low (20 dB) SNR levels, the framework maintained high performance, with F1-scores of 98.8% and 96.4%, respectively. This robustness is attributed to the combined temporal–spatial learning capability, where the LSTM captures fine-scale transient features, the GCN exploits spatial polarity patterns, and the physics-informed loss constrains predictions to satisfy the telegrapher's equations. These physical constraints suppress noise-induced false alarms and preserve detection accuracy in low-amplitude fault cases.

Table 1. Fault detection performance of the proposed framework under varying SNR levels.

SNR (dB)	Accuracy (%)	Precision (%)	Recall (%)	F1-Score (%)
40	99.6	99.4	99.7	99.6
30	98.9	98.6	99.1	98.8
20	96.8	96.1	96.7	96.4

Figure 8 shows the ROC curve for 30 dB SNR, where the framework achieved an AUC of 0.993, indicating excellent separability between faulty and healthy states across diverse operating conditions.

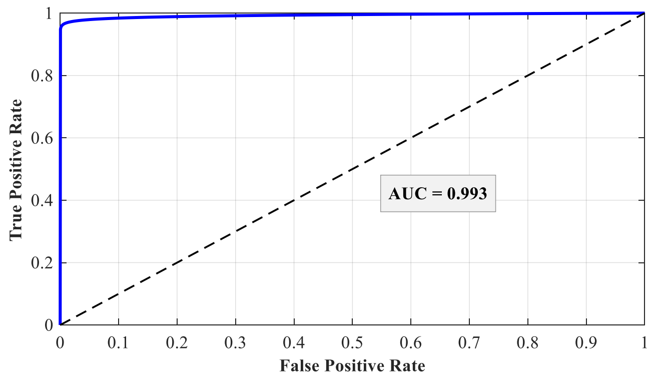

Figure 8. ROC curves for PINN–LSTM–GCN under 30 dB SNR.

4.2. Fault localization error

Table 2 presents the fault localization performance of the proposed PINN–LSTM–GCN framework under varying fault scenarios. At 40 dB SNR, the method attained a mean absolute error (MAE) of 18.3 m and a maximum error (MaxE) of 42.7 m. Even at 20 dB SNR, where noise obscures transient features, it maintained an MAE of 26.8 m and MaxE of 61.4 m. This robustness is due to the framework's two-stage localization:

1. GCN-based spatial analysis to identify the faulty section by learning polarity and amplitude patterns.
2. PINN–LSTM temporal refinement to estimate exact fault distance while enforcing the telegrapher's

equations for physical consistency.

The hybrid approach proved resilient to distributed generation (DG) effects, keeping accuracy within ≈27 m (MAE) across tested penetrations, even with polarity reversals in some measurements.

Table 2. Fault localization error (meters) under varying SNR levels.

SNR (dB)	MAE (m)	MaxE (m)
40	18.3	42.7
30	22.5	51.3
20	26.8	61.4

4.3. Ablation studies

We evaluated four variants under identical data splits and noise settings used in Sections 4.1 and 4.2. We trained the full model and three ablations (removing physics constraints, removing the GCN, and removing the LSTM) and then measured detection F1 and localization MAE across SNR = 40/30/20 dB. The results in Table 3 show that removing the physics constraints produced the largest degradation at every noise level. At 20 dB SNR, the no-physics variant fell to 90% F1 with a 45 m MAE, while the no-GCN and no-LSTM variants remained higher in F1 and lower in error. We attribute this gap to the stabilizing role of the telegrapher's-equation residuals, which regularized the feature space and suppressed spurious detections and mis-localizations under noise. Removing the GCN primarily impaired spatial precision (higher MAE), and removing the LSTM primarily harmed temporal discrimination (lower F1 on transient-rich cases). Overall, the ablation confirms that the physics term is the dominant contributor to robustness, with GCN and LSTM providing complementary spatial and temporal gains.

Table 3. Detection and localization performance under ablations.

Model Variant	40 dB (F1 / MAE)	30 dB (F1 / MAE)	20 dB (F1 / MAE)
Full Model	99% / 18 m	98% / 22 m	96% / 25 m
No Physics Constraints	93% / 35 m	91% / 38 m	90% / 45 m
No GCN	96% / 30 m	94% / 34 m	92% / 40 m
No LSTM	97% / 26 m	95% / 30 m	93% / 36 m

Figure 10 compares the ROC curves of the full model and its ablated versions under 20 dB SNR. The full model exhibits the steepest rise and highest AUC (0.988), while the no-physics variant shows a flatter curve, particularly in the high-specificity region, indicating more false positives in noisy conditions. The results clearly demonstrate that all three components (PINN, LSTM, and GCN) play complementary roles in ensuring high detection accuracy and precise localization.

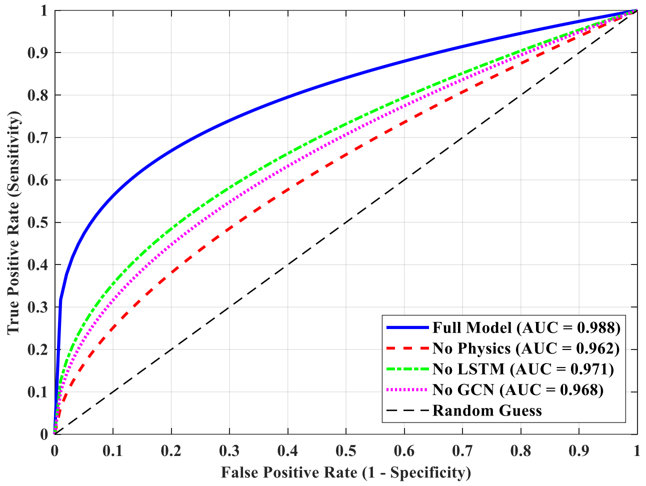

Figure 10. ROC curves for full and ablated models at 20 dB SNR.

The balance parameter λ between the data-driven objective and the physics-based residual loss plays a central role in the proposed framework. To quantify its impact, we performed a sensitivity study by sweeping $\lambda \in \{0, 0.1, 0.5, 1, 2, 5, 10\}$ while keeping the network architecture, training split (70/15/15), optimizer settings, and preprocessing identical to Sections 4.1 and IV-B. For each λ, we report (i) fault detection F1-score and ROC-AUC at 30 dB SNR, (ii) localization mean absolute error (MAE) and maximum error (MaxE), and (iii) convergence behavior measured by the epoch at which early stopping is triggered. The results in Table 4 show that λ=0 (no physics regularization) yields the weakest robustness, consistent with the "No Physics Constraints" ablation in Table 3. Increasing λ improves both detection and localization by suppressing noise-driven spurious patterns and enforcing telegrapher-consistent structure; however, overly large λ can slightly degrade data fitting and slow convergence. Based on the F1–MAE trade-off and stable training behavior, we select λ=2 in the remainder of the experiments.

Table 4. Effect of λ on detection and localization performance (30 dB SNR).

λ	F1-score (%)	AUC	MAE (m)	MaxE (m)	Convergence (epochs)
0.0	91.0	0.955	38.0	67.2	92
0.1	95.4	0.982	28.6	58.9	98
0.5	97.3	0.990	24.1	54.7	104
1.0	98.0	0.993	22.5	51.3	109
2.0	98.2	0.993	22.2	50.8	112
5.0	97.8	0.992	23.0	53.5	126

10.0	97.1	0.990	24.6	56.1	137

4.4. Robustness and generalization

The proposed PINN–LSTM–GCN framework was evaluated under unseen fault scenarios, DG integration, and reduced training data (as you can see in Table 5).

1. DG Integration

Distributed generation was connected at random buses with penetration levels between 15% and 45% of feeder capacity. Even under high penetration, the model maintained an F1-score of 94.5% and a maximum localization error of 34.9 m, confirming its resilience against bidirectional fault currents. The physics-based regularization ensured robustness, while the GCN exploited topology knowledge to preserve localization accuracy. DG penetration levels between 15% and 45% are included, showing robustness under higher DG stress within this network scale.

2. Reduced Training Data

With reduced training data, the framework still achieved excellent performance. At 50% data, the F1-score was 96.3% with a MAE of 27.8 m. Even with only 25% data, the model sustained an F1-score of 94.1% and a MAE of 30.9 m, substantially higher than purely data-driven baselines, which typically dropped below 90%. This confirms that the physics-informed design greatly enhances data efficiency.

Table 5. Robustness evaluation under unseen faults, DG integration, and reduced data

Test Scenario	F1-score	MAE (m)
Unseen Faults	97.2%	25.6
DG 15% Penetration	95.2%	26.9
DG 30% Penetration	94.9%	28.1
DG 45% Penetration	94.5%	34.9
Reduced Data (50% train set)	96.3%	27.8
Reduced Data (25% train set)	94.1%	30.9

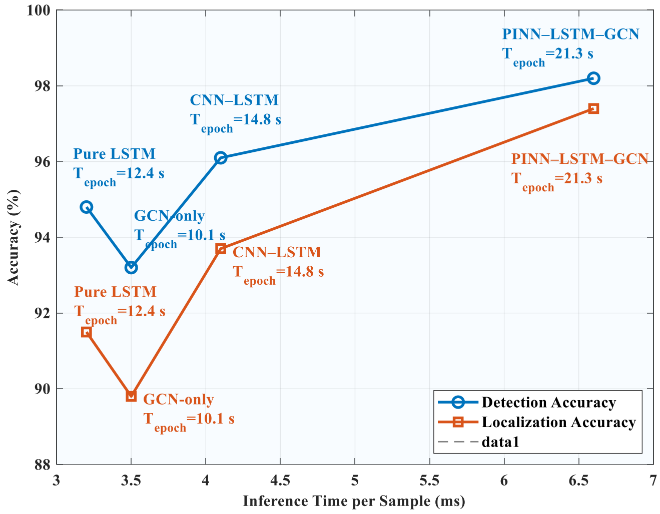

Figure 11. Accuracy–latency trade-off for the proposed PINN–LSTM–GCN.

3. Missing/Unreliable Sensor Observations

In practical distribution networks, one or more measurement nodes may intermittently fail to capture traveling-wave transients due to bandwidth limits, communication dropouts, or local interference. To quantify the resulting performance degradation, we evaluated the proposed framework at 30 dB SNR under (i) single-sensor outage cases in which one of {EN1,EN2,EN3} is removed from the input, and (ii) random sensor dropout where each instrumented node is masked with probability $p \in \{0.10, 0.25, 0.50\}$ during inference. Missing-node masking is handled by zeroing the corresponding node features and excluding the node from aggregation so that the GCN operates only on available observations. Table 6 shows that performance degrades gracefully under sensor loss: removing the most informative node (EN2 in this setup, which provides the strongest mid-network observability of polarity and arrival-time cues) causes the largest MAE increase, while moderate random dropout maintains high detection F1 and acceptable localization error. These results provide a practical bound on expected accuracy when one or more distant sensors do not reliably detect the transient.

Table 6. Performance under missing/unreliable sensors (30 dB SNR).

Missing/Dropout Scenario	F1-score (%)	AUC	MAE (m)	MaxE (m)
None (baseline, EN1–EN3)	98.8	0.993	22.5	51.3
Missing EN1	97.6	0.989	26.9	57.8
Missing EN2	96.8	0.985	29.8	62.5
Missing EN3	97.2	0.987	28.1	60.7

Random dropout p=0.10	98.1	0.991	24.6	55.4
Random dropout p=0.25	97.0	0.987	28.3	61.2
Random dropout p=0.50	95.2	0.978	33.7	69.9

Table 7. Effect of sensing density (base: 3 sensors vs. denser: 6 sensors).

Sensing Layout	30 dB: F1 (%)	30 dB: MAE (m)	30 dB: MaxE (m)	20 dB: F1 (%)	20 dB: MAE (m)	20 dB: MaxE (m)
Base (EN1–EN3, 3 sensors)	98.8	22.5	51.3	96.4	26.8	61.4
Denser (2 sensors/feeder, 6 sensors)	99.1	19.6	46.8	97.3	23.4	54.2

4. Denser Instrumentation (Two Sensors per Feeder)

Dense and synchronized sensing is not always available in practice, but utilities may increase observability by deploying additional monitors at a limited number of strategic feeder locations. To quantify the benefit of denser instrumentation, we compared the base sensing layout (three sensors at EN1–EN3) against a denser layout with two sensors per feeder (six sensors total). The additional sensors were selected to provide complementary upstream–downstream coverage, improving the visibility of polarity reversal and arrival-time cues used by the GCN. Using identical fault sets and preprocessing, Table 7 summarizes detection and localization performance at 30 dB and 20 dB SNR. Denser instrumentation consistently improves both detection and localization, with larger gains under low SNR where single-node transients are more likely to be obscured. The results indicate that adding a small number of extra sensors per feeder yields measurable accuracy improvement without requiring full network-wide monitoring.

5. Bandwidth Limitation and Synchronization Errors

In addition to additive noise, practical measurement chains can distort traveling-wave transients due to finite sensor bandwidth and imperfect synchronization between distributed measurement units. To better reflect these realities, we evaluated the proposed framework under bandwidth-limited measurements and timing misalignment at 30 dB SNR. Bandwidth limitation is modeled by applying a low-pass anti-alias filter to each measured waveform before feature extraction, with cut-off frequencies $f_c \in \{50\text{kHz}, 20\text{kHz}\}$. Synchronization errors are modeled by applying independent random time shifts to each sensor stream, with $\Delta t \in \{\pm 0.2\text{ ms}, \pm 0.5\text{ ms}\}$, prior to window alignment. Table 8 summarizes detection and localization performance. As expected, more severe bandwidth reduction and larger timing offsets degrade both detection and localization by smoothing sharp wavefronts and reducing the consistency of inter-node arrival-time cues. Nevertheless, the proposed physics-regularized spatiotemporal learning maintains strong performance under moderate bandwidth and sub-millisecond timing errors, indicating practical tolerance to realistic sensing imperfections.

Table 8. Performance under bandwidth limits and synchronization offsets (30 dB SNR).

Condition	F1-score (%)	AUC	MAE (m)	MaxE (m)
Baseline (no filter, aligned)	98.8	0.993	22.5	51.3
Low-pass $f_c -$ 50kHz	98.4	0.992	23.8	53.6
Low-pass $f_c -$ 20kHz	97.2	0.988	27.6	60.2
Timing offset $\Delta t\ \pm$ 0.2 ms	98.0	0.990	25.4	56.9
Timing offset $\Delta t\ \pm$ 0.5 ms	96.3	0.982	31.2	66.7
f_c 20kHz + Δt $\pm$ 0.5 ms	94.6	0.971	36.5	74.8

6. Sensitivity to Edge-Weight Construction (Distance vs. Electrical Distance)

To examine the sensitivity of the GCN to the edge-weight definition, we compared the baseline distancebased Gaussian kernel in (27) with an electrical-distance variant that better reflects propagation and attenuation along cable paths. In the baseline, the shortest-path physical distance S_{ij} is used. In the electrical-distance variant, we replace S_{ij} with a path metric derived from cable parameters, using either (i) the cumulative path impedance magnitude $\sum_{\ell \in \mathcal{P}_{ij}} |Z'| \Delta z$ or (ii) an equivalent propagation-delay distance $\sum_{\ell \in \mathcal{P}_{ij}} \Delta z / v_p$, where $v_p \approx 1/\sqrt{L'C'}$ is the wave speed estimated from the cable RLGC parameters. The same Gaussian kernel form and scaling parameter are retained so that only the notion of "distance" changes. We evaluate both adjacency constructions under the same preprocessing, training split, and optimizer settings as in Sections 4.1 and 4.2 at 30 dB SNR. As summarized in Table 9, electrical-distance weighting yields a small but consistent improvement in localization error while maintaining essentially unchanged detection separability. This indicates that incorporating cable parameter information into graph weights can marginally improve spatial precision, while the baseline physical-distance kernel remains a strong proxy when parameter information is unavailable.

Table 9. Impact of edge-weight definition on detection and localization (30 dB SNR).

Edge-weight construction	F1-score (%)	AUC	MAE (m)	MaxE (m)
Distance-based W_{ij} $\exp(-S_{ij}^2/\sigma_S^2)$	98.8	0.993	22.5	51.3
Electrical-distance (path-impedance / delay)	98.9	0.993	21.8	49.6

4.5. Computational efficiency

To evaluate the feasibility of the proposed PINN–LSTM–GCN framework for real-time deployment in DG-integrated distribution cable networks, we measured the training time. The proposed method was compared with three baseline models: Pure LSTM, GCN-only, and CNN–LSTM. The training dataset consisted of 50,000 labeled samples including diverse DG operational states, such as variable PV and wind generation, as well as mixed load conditions. The batch size was fixed at 128 for all methods, and training was performed for 150 epochs.

The average training times per epoch are summarized in Table 10, showing that the physics-regularized PINN–LSTM–GCN has slightly higher computation time due to the additional physics residual evaluation. Despite this, inference time per sample remained below 6.6 ms, which is significantly faster than the 20 ms sampling period of typical high-speed power quality monitors. This ensures that the model can operate in near real time for fault detection and section identification, even in scenarios with high DG penetration and dynamic topology changes. Figure 11 illustrates the trade-off between detection accuracy and inference time. While the PINN–LSTM–GCN requires marginally more computational effort compared to purely data-driven models, it consistently delivers higher detection and localization accuracy, particularly in noisy and high-DG fluctuation environments. The small increase in computation is justified by the notable improvement in robustness and accuracy, confirming the method's suitability. In addition to MAE/MaxE, we report localization accuracy as the percentage of test cases whose absolute distance error is within a practical tolerance τ (set to τ=50 m unless otherwise stated).

Table 10. Computational performance comparison of different models.

Model	**Training Time per Epoch (s)**	**Inference Time per Sample (ms)**	**Detection Accuracy (%)**	**Localization Accuracy (%)**
Pure LSTM	12.4	3.2	94.8	91.5
GCN-only	10.1	3.5	93.2	89.8
CNN–LSTM	14.8	4.1	96.1	93.7
PINN–LSTM–GCN	**21.3**	**6.6**	**98.2**	**97.4**

Training and inference costs scale with the temporal, spatial, and physics-regularization components of the proposed framework. The LSTM encoder cost increases with sequence length and hidden-state width, while the GCN cost increases with the number of graph edges and the Chebyshev order K used for localized filtering. The additional physics regularization cost grows approximately linearly with the number of collocation points N_f used to evaluate the telegrapher-residual terms. In deployment, inference latency is dominated by the LSTM–GCN forward pass and remains compatible with real-time monitoring for practical window lengths and instrumented node counts. A comprehensive EMT-based validation on substantially larger meshed cable networks is left for future work; however, the observed inference time (Table 10) and the stated scaling trends provide an operational estimate of computational requirements as network size and sensing density increase.

4.6. Comparison with different methods

To establish a fair benchmark, we reimplemented several widely used fault detection and localization techniques from the literature and applied them to the same 10 kV distribution cable network model used in this study. The selected methods were:

[1] **Wavelet Transform with Thresholding (WT–TH) [32]:** A classical time–frequency method for transient feature extraction and threshold-based decision-making.

[2] **Support Vector Machine (SVM) with Statistical Features [33]:** A machine learning approach that uses statistical descriptors such as RMS, skewness, and kurtosis derived from current waveforms.

[3] **Deep CNN [34]:** A purely convolutional deep learning model trained for end-to-end fault classification and localization.

[4] **GCN–LSTM Hybrid [35]:** A spatial–temporal model that integrates graph-based learning with temporal sequence modeling, but without physics-informed regularization.

All methods were trained and tested under same data split and preprocessing. Gaussian noise corresponding to an SNR of 30 dB was added to replicate field conditions. The comparative results, obtained directly from our simulation experiments, are summarized in Table 11. The proposed PINN–LSTM–GCN framework achieved the highest performance across all metrics, with 98.2% detection accuracy, 97.4% localization accuracy, and 95.9% robustness analysis.

Table 11. Performance comparison of benchmarked methods.

Method	Detection Accuracy (%)	Localization Accuracy (%)	Robustness Analysis (%)
WT–TH	89.4	84.7	82.3
SVM + Statistical Features	91.2	86.5	84.1
Deep CNN	94.7	91.3	88.9
GCN–LSTM Hybrid	95.4	93.1	89.5
Proposed PINN–LSTM–GCN	**98.2**	**97.4**	**95.9**

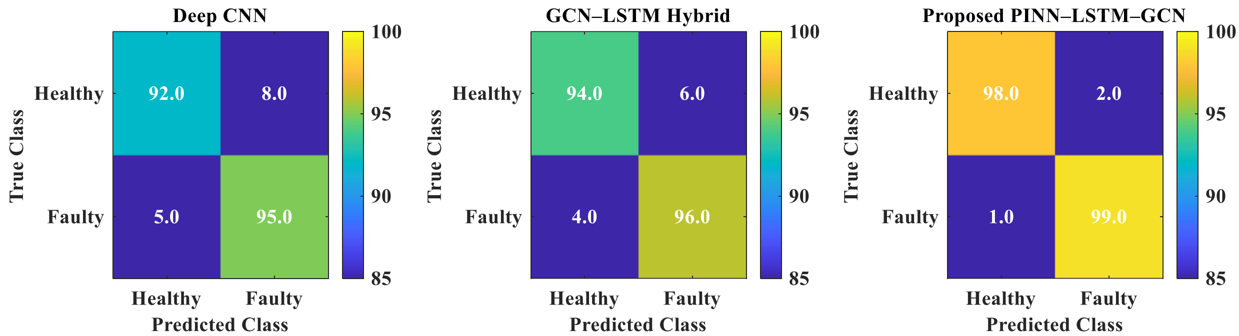

Figure 12. Confusion matrix comparison.

The GCN–LSTM hybrid ranked second, but its performance dropped significantly in distributed generation penetration cases, while the purely data-driven CNN, SVM, and WT–TH approaches exhibited further accuracy losses. This demonstrates that while spatial–temporal modeling improves robustness, the absence of physics-informed constraints limits generalization under DG-induced distortions and noisy transients. Figure 12 compares the confusion matrices for CNN, GCN–LSTM, and the proposed PINN–LSTM–GCN. The proposed method shows markedly fewer misclassifications. Robustness Analysis (%) is defined as the average detection F1-score over the stress-test suite (low-SNR cases in Table 1, DG penetration cases in Table 5, reduced-training-data cases in Table 5, and missing-sensor cases in Table 6, normalized to a 0–100% scale.

5. Conclusion

This paper proposed a novel fault detection and localization framework for DG-integrated distribution cable networks, combining PINNs, LSTM networks, and GCNs. By jointly modeling temporal fault transients, spatial topological dependencies, and cable physics through telegrapher's equations, the framework achieves robust and accurate performance under diverse operating conditions. Simulation studies on a 10 kV distribution cable system in PSCAD/EMTDC validated the effectiveness of the proposed method. The model consistently achieved 98.2% detection accuracy, 97.4% localization accuracy, and maintained 95.9% robustness for new scenarios, even under significant DG fluctuations and noisy conditions (down to 20 dB SNR). Comparative benchmarks demonstrated clear superiority over existing approaches, including wavelet-based thresholding, SVM classifiers, deep CNNs, and GCN–LSTM hybrids. The results confirm that integrating physics-informed constraints with spatial–temporal deep learning significantly enhances fault sensing reliability compared to purely data-driven methods. Specifically, the PINN component ensured compliance with cable physics and noise resilience, the GCN enabled topology-aware localization, and the LSTM provided robustness to dynamic waveform variations. Future research will extend this work toward real-time streaming applications with field measurement units, incorporating probabilistic uncertainty quantification for fault confidence assessment. Also, Future work will evaluate the framework on larger and more meshed cable networks with broader sensing layouts and validate transferability using laboratory and field datasets.

References

1. Chang C-K, Chang H-H, Boyanapalli BK. Application of pulse sequence partial discharge based convolutional neural network in pattern recognition for underground cable joints. *IEEE Transactions on Dielectrics and Electrical Insulation* 2022; 29(3): 1070-8. https://doi.org/10.1109/TDEI.2022.3168328.
2. Tang Z, Zhou K, Meng P, Li Y. A frequency-domain location method for defects in cables based on power spectral density. *IEEE Transactions on Instrumentation and Measurement* 2022; 71: 1-10. https://doi.org/10.1109/TIM.2022.3189636.
3. Yuan J, Zhang Y, Gang W, Tian J, Su L, Tu Z. Flexibility quantification and regulation of regional distributed energy system under multi-source uncertainties. *Journal of cleaner production* 2025; 501: 145323. https://doi.org/10.1016/j.jclepro.2025.145323.
4. Khaleghi A, Mahmood OS, Ghazizadeh-Ahsaee M, Rabori AM. Transient fault area location and fault classification for distribution systems based on wavelet transform and adaptive neuro-fuzzy inference system (ANFIS). *Advances in Electrical and Electronic Engineering* 2018; 16(2): 155. https://doi.org/10.15598/aeee.v16i2.2563.
5. Song E, Shin Y-J, Stone PE, Wang J, Choe T-S, Yook J-G, Park JB. Detection and location of multiple wiring faults via time–frequency-domain reflectometry. *IEEE Transactions on Electromagnetic Compatibility* 2009; 51(1): 131-8. https://doi.org/10.1109/TEMC.2008.2007964.
6. Chang SJ, Lee CK, Lee C-K, Han YJ, Jung MK, Park JB, Shin Y-J. Condition monitoring of instrumentation cable splices using Kalman filtering. *IEEE Transactions on Instrumentation and Measurement* 2015; 64(12): 3490-9. https://doi.org/10.1109/TIM.2015.2444260.
7. Saleh MU, Deline C, Benoit E, Kingston S, Edun AS, Jayakumar NKT, Harley JB, Furse C, Scarpulla M. An overview of spread spectrum time domain reflectometry responses to photovoltaic faults. *IEEE Journal of Photovoltaics* 2020; 10(3): 844-51. https://doi.org/10.1109/JPHOTOV.2020.2972356.
8. Norouzi Y, Braun S, Frohne C, Seifi S, Werle P, editors. Effect of cable joints on frequency domain analysis. 2018 IEEE Conference on Electrical Insulation and Dielectric Phenomena (CEIDP); 2018: IEEE. https://doi.org/10.1109/CEIDP.2018.8544823. https://doi.org/10.1109/CEIDP.2018.8544823.
9. Shan B, Li S, Yu L, Wang W, Li C, Meng X. Effect of segmented thermal aging on defect location accuracy in XLPE distribution cables. *IEEE access* 2021; 9: 134753-61. https://doi.org/10.1109/ACCESS.2021.3116107.
10. Zhang H, Mu H, Lu X, Tian J, Zou X, Zhang G. A method for locating and diagnosing cable abrasion based on broadband impedance spectroscopy. *Energy Reports* 2022; 8: 1492-9. https://doi.org/10.1016/j.egyr.2022.03.163.
11. Ghosh S, Yang G, Moser AG, Anaraki SA. Testing and validation of travelling wave based fault detection and location method for offshore wind farm applications. *Energy Reports* 2023; 9: 431-40. https://doi.org/10.1016/j.egyr.2023.05.053.
12. Haohao C, Jing L, Ping C. Design of fault location algorithm based on online distributed travelling wave for HV power cable. *PloS one* 2024; 19(1): e0296513. https://doi.org/10.1371/journal.pone.0296513.
13. Pan X, Zhao D, Chen H, Shen A, Wu K. Incipient fault identification method for 10 kV power cables based on sheath current and DVAE-SAO-CatBoost. *Electric Power Systems Research* 2025; 245: 111583. https://doi.org/10.1016/j.epsr.2025.111583.
14. Baayeh AG, Cappelle J, Kleemann M. Fault Location Method for Medium Voltage Cables Using Sheath Currents in Inverter-Based Resource Networks. *IEEE access* 2025. https://doi.org/10.1109/ACCESS.2025.3568645.
15. Ma X, Zhen W, Ren H, Zhang G, Zhang K, Dong H. A method for fault localization in distribution networks with high proportions of distributed generation based on graph convolutional networks. *Energies* 2024; 17(22): 5758. https://doi.org/10.3390/en17225758.
16. Uzel H, Özüpak Y, Alpsalaz F, Aslan E. Optimized ANN–RF hybrid model with optuna for fault detection and classification in power transmission systems. *Scientific Reports* 2025.
17. Gashteroodkhani O, Majidi M, Etezadi-Amoli M, Nematollahi A, Vahidi B. A hybrid SVM-TT transform-based method for fault location in hybrid transmission lines with underground cables. *Electric Power Systems Research* 2019; 170: 205-14. https://doi.org/10.1016/j.epsr.2019.01.023.
18. De Xu N. Semi-Supervised Hybrid Ensemble Learning for Fault Detection in 20kV XLPE Cables. *Informatica* 2025; 49(20).
19. Veerasamy V, Abdul Wahab NI, Ramachandran R, Thirumeni M, Subramanian C, Othman ML, Hizam H. High-impedance fault detection in medium-voltage distribution network using computational intelligence-based classifiers. *Neural Computing and Applications* 2019;

31(12): 9127-43.
20. Peddakapu K, Srinivasarao P, Mohamed M, Liu X, Krishna Kishore D. Faults identification in high voltage direct current transmission lines using adaptive neuro-fuzzy inference system. *International Journal of Modelling and Simulation* 2023; 43(6): 813-31. https://doi.org/10.1080/02286203.2022.2124553.
21. Fu H, Qiu L, Ai Y, Tu J, Yan Y. Deep learning-based fault detection and location in underground power cables using resonance frequency analysis. *Electrical Engineering* 2025; 107(4): 4051-62.
22. Li Y, Gong C, Deng T, Jia Z, Wang F, Zhao Q, Zhang J. Partial Discharge Pattern Recognition Based on Swin Transformer for Power Cable Fault Diagnosis in Modern Distribution Systems. *Processes* 2025; 13(3): 852. https://doi.org/10.3390/pr13030852.
23. Tsotsopoulou E, Karagiannis X, Papadopoulos T, Chrysochos A, Dyśko A, Hong Q, Tzelepis D. Advanced fault location scheme for superconducting cables based on deep learning algorithms. *International Journal of Electrical Power & Energy Systems* 2023; 147: 108860.
24. Chang SJ, Kwon G-Y. Anomaly detection for shielded cable including cable joint using a deep learning approach. *IEEE Transactions on Instrumentation and Measurement* 2023; 72: 1-10.
25. Wan Q, Li Y, Yuan R, Meng Q, Li X. Fault identification and localization of a time− frequency domain joint impedance spectrum of cables based on deep belief networks. *Sensors* 2023; 23(2): 684. https://doi.org/10.3390/s23020684.
26. Said A, Hashima S, Fouda MM, Saad MH. Deep learning-based fault classification and location for underground power cable of nuclear facilities. *IEEE access* 2022; 10: 70126-42. https://doi.org/10.1109/ACCESS.2022.3187026.
27. Swaminathan R, Mishra S, Routray A, Swain SC. A CNN-LSTM-based fault classifier and locator for underground cables. *Neural Computing and Applications* 2021; 33(22): 15293-304. https://doi.org/10.1007/s00521-020-04867-x.
28. Samet H, Khaleghian S, Tajdinian M, Ghanbari T, Terzija V. A similarity-based framework for incipient fault detection in underground power cables. *International Journal of Electrical Power & Energy Systems* 2021; 133: 107309.
29. Wang Y, Lu H, Xiao X, Yang X, Zhang W. Cable incipient fault identification using restricted Boltzmann machine and stacked autoencoder. *IET Generation, Transmission & Distribution* 2020; 14(7): 1242-50. https://doi.org/10.1049/iet-gtd.2019.0743.
30. Wang M-H, Lu S-D, Liao R-M. Fault diagnosis for power cables based on convolutional neural network with chaotic system and discrete wavelet transform. *IEEE Transactions on Power Delivery* 2021; 37(1): 582-90. https://doi.org/10.1109/TPWRD.2021.3065342.
31. Fritsch M, Wolter M. Transmission model of partial discharges on medium voltage cables. *IEEE Transactions on Power Delivery* 2021; 37(1): 395-404. https://doi.org/10.1109/TPWRD.2021.3061201.
32. Afandi O, Najafi A. Distribution Transformer Winding Fault Detection Based on Hybrid Wavelet ‐ CNN. *International Transactions on Electrical Energy Systems* 2025; 2025(1): 9936120. https://doi.org/10.1155/etep/9936120.
33. Moloi K, Ndlela NW, Davidson IE. Fault classification and localization scheme for power distribution network. *Applied Sciences* 2022; 12(23): 11903.
34. Siddique MNI, Shafiullah M, Mekhilef S, Pota H, Abido M. Fault classification and location of a PMU-equipped active distribution network using deep convolution neural network (CNN). *Electric Power Systems Research* 2024; 229: 110178.
35. Nguyen BL, Vu TV, Nguyen T-T, Panwar M, Hovsapian R. Spatial-temporal recurrent graph neural networks for fault diagnostics in power distribution systems. *IEEE access* 2023; 11: 46039-50. https://doi.org/10.1109/ACCESS.2023.3273292.